Ultrasonic Wavefield Imaging

2

Jennifer E. Michaels

Contents

Abstract

Ultrasonic wavefield imaging, or the acquisition and subsequent analysis of wave motion generated by a fixed source, is a powerful research tool that is also being considered for nondestructive evaluation (NDE). Many proposed wavefield-based NDE methods have come from the structural health monitoring (SHM) community and are based upon guided waves. If guided wave transducers are already embedded in or mounted on a structure as part of an SHM system, then wavefield-based inspection can potentially take place with very little required disassembly. Wavefield inspection methods may also be practical for stand-alone inspection because of the richness of the data and the noncontact nature of most

J. E. Michaels (✉)
School of Electrical and Computer Engineering, Georgia Institute of Technology, Atlanta, GA, USA
e-mail: jemichaels@gatech.edu

N. Ida, N. Meyendorf (eds.), *Handbook of Advanced Nondestructive Evaluation*,
https://doi.org/10.1007/978-3-319-26553-7_18

implementations. In its simplest form, wavefield imaging is a very effective method for visualizing wave motion on the surface of a specimen. However, for it to become a practical NDE method, analysis methods must be applied to the wavefield data to yield quantitative information concerning the detection, localization, and characterization of damage. The focus of this chapter is to provide an introduction to the acquisition and analysis of wavefield data in the context of three case studies: impact damage in composites, bond evaluation for aluminum plates, and characterization of scattering from notched through-holes. References to additional methods and applications are given for the interested reader.

Introduction

The intuitive value of ultrasonic wave imaging (UWI) can be readily appreciated by anyone who has watched water waves in a pond or lake resulting from a point-like disturbance. Both the nature of wave propagation and the interactions of the waves with obstacles are clearly visible. When applied to nondestructive evaluation (NDE), UWI provides a means to not only evaluate how waves propagate in a specimen of interest but also how they interact with both structural features and defects. Watching a "movie" of wave motion resulting from a stationary source of ultrasonic waves provides qualitative insight that can lead to improved inspection methods, and subsequent analysis of the wavefield data can provide quantitative information regarding both material properties and damage.

As is the case for conventional pulse-echo and through-transmission data acquisition with an automated scanning system, wavefield data are typically acquired by repetitively exciting the source and moving the receiver in a raster pattern over the accessible surface of the part. Unlike conventional ultrasonic methods, the source is stationary and only the receiver moves from point-to-point. The raster scanning process enables the complete wavefield to be acquired over a region of interest. Wavefield visualization occurs by displaying the data as a movie; that is, as a series of spatial frames or "snapshots" that update as time advances. In this manner one can view the waves propagating outward from the source and subsequently interacting with geometrical features and damage. Although various implementations of wavefield imaging have existed for many years (Wyatt 1972; Hall 1977; Nishizawa et al. 1997), the widespread availability of laser Doppler vibrometers that can acquire signals in the high kHz and low MHz range has led to a rapid expansion of research and development utilizing full wavefield data.

UWI is perhaps most suited to the measurement of guided waves since their propagation is guided by the accessible surface, which is also the measurement surface for wavefield acquisition. Guided waves are frequently used as an NDE screening method because of their ability to propagate long distances and remain sensitive to damage, but their long wavelengths relative to critical flaw sizes make damage characterization challenging. Wavefield imaging has greatly contributed to the understanding of how guided waves propagate and interact with damage such as fatigue cracks, impacts, and corrosion. Researchers in the area of structural health

monitoring (SHM), also referred to as in situ NDE, are proposing arrays of permanently attached transducers to continuously monitor critical structures using guided waves. If such an SHM system generates an alarm, a more thorough inspection will be required. Using one or more of the attached SHM transducers as sources of guided waves for UWI has thus been proposed as a follow-up NDE method that has the desirable characteristic of being noncontact (Michaels and Michaels 2006; Gannon et al. 2015).

Application of UWI to bulk waves is also possible, but the recorded data captures only the portion of the wavefield that interacts with the accessible surface, primarily by reflection but also via skimming waves. Nevertheless, it is possible to extract quantitative information from the wavefield regarding both propagation and scattering. Since conventional ultrasonic inspection methods have the same measurement limitation, it is reasonable to expect that application of UWI to bulk waves can yield information relevant to NDE.

This chapter aims to describe UWI in the context of NDE and demonstrate its application via several case studies; it is an expanded version of the conference proceedings by Michaels (2017). Advancement of UWI methods is rapid with many researchers worldwide actively engaged in developing methods, so the material presented here should not be considered as an exhaustive treatment but rather as an introduction. This chapter is organized as follows. Practical information on the acquisition and visualization of wavefield data is first discussed. Then, several analysis methods are described and illustrated using experimental wavefield data. Next, three case studies are presented that relate to detection and characterization of damage, two with guided waves and one with bulk waves. A brief review of other recent work is then provided to augment what is presented here. Finally, concluding remarks are made summarizing the status of wavefield imaging as an NDE method.

Acquiring and Visualizing Ultrasonic Wavefield Data

The most common setup for acquiring wavefield data is to affix a piezoelectric transducer to the specimen of interest and record the resulting wave motion with a laser Doppler vibrometer (LDV). The LDV can either be attached to an XY scanner or it can be part of a scanning mirror system that directs the laser beam by tilting a mirror. A scanner-based LDV system is usually assembled by purchasing and integrating components, which include the scanner, a single-point laser vibrometer, a digitizer, and equipment such as a pulser-receiver or function generator to excite the wave source. A computer and appropriate software are required to complete the system. A mirror-based system is usually procured as a complete system including software that does not require integration or customization. Regardless of the specific LDV system, the resulting data consists of a set of signals that are proportional to the displacement or velocity of the wave motion, which for the most commonly used single-head LDV is out-of-plane motion. Three-axis LDVs are also available that measure all three displacement components, but the additional complexity and cost of these systems make them much less practical for use outside of the laboratory.

For either the scanner-based or mirror-based single-head LDV configuration, it can be challenging to obtain a good signal-to-noise ratio (SNR), and careful surface preparation is usually required. For lower frequencies (i.e., under 1 MHz), many laboratories have successfully used retro-reflective automotive tape, which is applied to the surface on which the laser vibrometer acquires data. This type of tape is particularly suited for a mirror-based LDV system because the laser beam is not perfectly normal to the surface over the entire scanning area. For a scanner-mounted LDV, the normality of the laser beam can be better controlled and other surface preparations that provide a strong specular reflection can be used. These can include surface polishing (for metallic specimens), reflective paint, and other types of reflective tape. Signal averaging is also typically applied to further improve the SNR, but there is a trade-off with acquisition time. As expected, for higher frequencies the presence of any additive surface preparation can disturb the wave propagation and hence affect the recorded signals.

Another relatively common means of obtaining wavefield data is to use an air-coupled transducer as a receiver instead of the LDV, which has the advantages of lower cost and faster scan speeds, but presents several disadvantages, mainly related to data quality because of the large impedance mismatch between air and the specimen under test. Also, an air-coupled system does not directly measure surface motion but records airborne waves that have leaked from the specimen and propagated to the transducer. Completely noncontact systems have also been developed in which waves are generated by a fixed laser or air-coupled transducer and measured by a scanned LDV. An alternative approach is to generate waves with a scanned laser and receive with either a fixed piezoelectric transducer or a fixed LDV; the waves appear to originate at the fixed receiver location due to reciprocity of transmission and reception for linear elastodynamic systems. The laser source can also be scanned and the receiver fixed. These laser-based noncontact systems are described and compared by An et al. (2013). Lee et al. (2014) evaluated combined laser and air-coupled noncontact systems in which a scanned laser source generates waves that are measured with either a piezoelectric or capacitive air-coupled transducer. Although the use of a laser to generate ultrasonic waves has several advantages, it presents the disadvantages of safety issues, possible surface damage, and additional system complexity.

Ultrasonic wavefield data are by definition acquired in both time (one dimension) and space (one or two dimension). When acquired in one spatial dimension, the wavefield data can be represented as $w(t,r)$, where t is time and r is the single spatial dimension. A series of time signals are typically acquired along a line, although any curve could be the acquisition path, and these 2-D wavefields are referred to as either line scans or B-scans. An ultrasonic wavefield acquired in two spatial dimensions can be represented as $w(t,x,y)$, where x and y are the two spatial dimensions on the surface of the specimen, and these 3-D wavefields are referred to as area scans. The signals comprising the wavefield are typically acquired on a rectilinear grid with equal spatial sampling increments in both spatial dimensions. Line scans can be readily extracted from area scans.

The simplest analysis method is wavefield visualization in two dimensions in the form of images. For line scans, the two dimensions are time and space, and the images show the trajectories of the measured waves. For area scans, data can be visualized by extracting line scans along any desired direction, but it is difficult to visualize the entire wavefield in this manner. The most effective visualization method for area scans is to view the wavefield as a movie. Although data are acquired by repeatedly exciting the fixed source and measuring the response at different spatial locations, the entire wavefield is best visualized by showing a series of 2-D images as time progresses, enabling the propagating wavefield to be viewed as a movie. Each frame is an *x*-*y* image at a fixed time, which is also called a "snapshot."

Figure 1 shows both a photograph and a drawing of an impact-damaged composite panel specimen from which laser vibrometer data were acquired. The panel measured 460 × 460 × 2.5 mm and was nominally homogeneous with an orthotropic layup of $[0/90]_4$. The photograph of Fig. 1a shows the transducer side of the panel on which six lead zirconate titanate (PZT) disks were attached with epoxy and covered with a bubble-filled epoxy mixture for protection. These radially polarized disks with a center frequency of 300 kHz were the sources of waves and were each 7 mm in diameter and 0.5 mm in thickness. Retro-reflective tape was applied to the other side of the panel over the area shown by the box in Fig. 1b, and laser vibrometer data were recorded over this 219 × 249 mm region at an increment of 1.5 mm. Signals were digitized at 20 MHz and subsequently down-sampled to 5 MHz during post-processing. The total scan time was about 6 h, which works out to a little less than 1 s per point, and included extensive time averaging to increase the SNR.

Typical wavefield snapshots are shown in Fig. 2 for the case of transducer #1 as the source and with a 50–500 kHz chirp excitation. Data were processed prior to generating the plots to obtain the equivalent response to an impulsive excitation

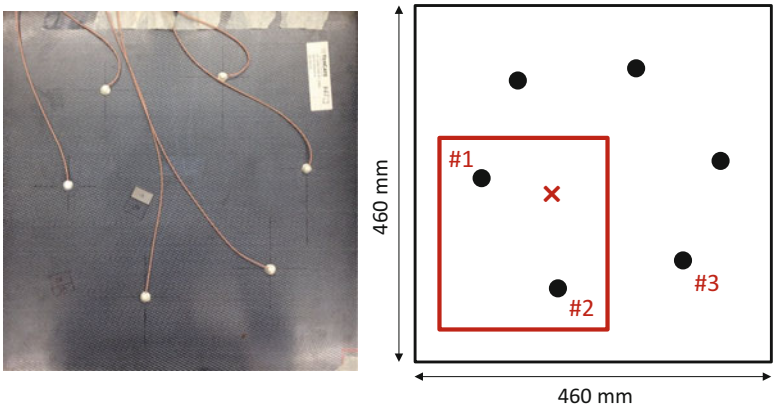

Fig. 1 Composite panel specimen (**a**) photograph and (**b**) diagram. The box indicates the wavefield scan area and the "×" designates the impact location

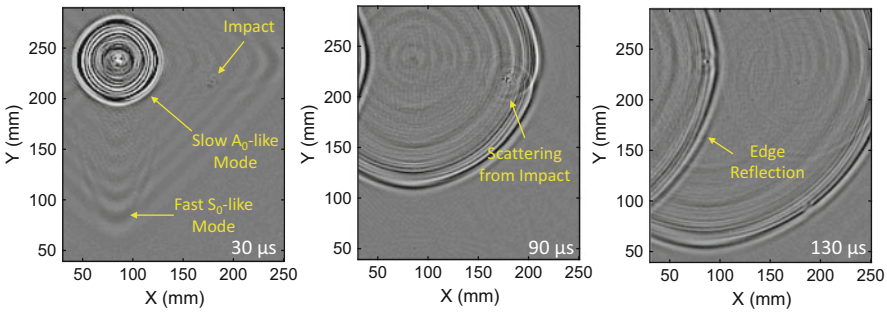

Fig. 2 Wavefield snapshots from the composite panel specimen at times of (**a**) 30 μs, (**b**) 90 μs, and (**c**) 130 μs

within the chirp bandwidth (Michaels et al. 2013). In the 30 μs snapshot, it can be seen that the weak faster mode is very anisotropic with almost square wavefronts. In the 90 μs snapshot, the slower mode has just passed the impact site and both scattering and energy trapping are evident. In the 130 μs snapshot, a reflection of the slower mode from the left edge can be seen. Although scattering from the impact site is clearly visible, the wavefield is dominated by both the incident waves and edge reflections. Visualization of UWI data as either a series of snapshots or a movie provides a very useful and intuitive means of understanding how waves propagate in a specimen, but such visualization does not provide a quantitative assessment of damage.

Analyzing Ultrasonic Wavefield Data

A variety of analysis techniques can be applied to UWI data with the goal of extracting quantitative NDE results. The concepts of phase and group velocity are first reviewed as applied to both guided and bulk UWI data. Then two energy imaging methods are defined and demonstrated using the composite panel data. Finally, Fourier domain (frequency-wavenumber) methods are described and illustrated, also with the composite panel data.

Phase and Group Velocities

When analyzing guided wavefields, one must be cognizant of the difference between group velocity and phase velocity, which is caused by geometric dispersion (Rose 1999). Figure 3a shows LDV data acquired from a 1-D scan (in space) of guided waves propagating in a 2.54 mm thick aluminum plate. In this B-scan (time-distance) presentation, the time axis does not correspond to depth within the part, as is the case for a conventional B-scan, but to the propagation time from the source to the spatial location. The two fundamental Lamb wave modes are present, the faster S_0 mode and the slower A_0 mode, and their theoretical phase velocity

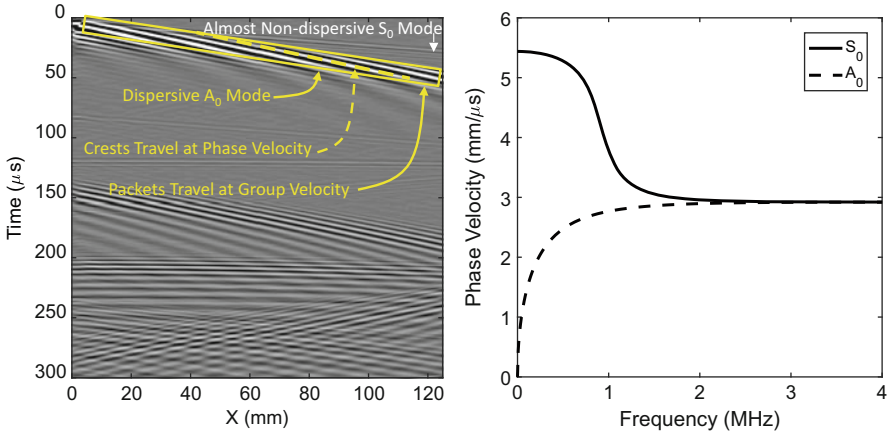

Fig. 3 (**a**) Wavefield data recorded from a 2.54 mm thick aluminum plate, and (**b**) the theoretical dispersion curves for the two fundamental guided wave modes

dispersion curves are shown in Fig. 3b. The S_0 mode appears much weaker than the A_0 mode because its out-of-plane displacement on the measurement surface is quite small compared to its in-plane displacement. The S_0 mode is largely nondispersive with the group velocity of the wave packet traveling at essentially the same speed as the peaks and valleys, which travel at the phase velocity. The slower A_0 mode is strongly dispersive, and it can be clearly seen that the wave packet is traveling faster than the peaks and valleys; i.e., the group velocity c_g is faster than the phase velocity c_p.

The situation is different when acquiring bulk wave signals, which propagate in the bulk material and are not guided by the specimen surfaces. Geometric dispersion does not apply to bulk waves, and the direction of propagation is typically either oblique or normal to the surface rather than parallel to the surface as is the case for guided waves. For example, if wavefield data are recorded from normally incident longitudinal waves, the entire wavefront hits the measurement surface at the same time, resulting in an apparent phase velocity of infinity. In general, for a refracted angle of θ_r, as illustrated in Fig. 4, the apparent wavelength on the surface is elongated and the apparent phase velocity on the surface is increased by a factor of $\sin(\theta_r)$; that is,

$$c_p = \frac{c}{\sin(\theta_r)}, \tag{1}$$

where c is the shear or longitudinal bulk wave speed and c_p is the apparent phase velocity on the specimen surface. The apparent group velocity on the surface is generally not of interest for bulk wavefield data since data are not measured along the direction of propagation and the apparent group velocity is generally a function of measurement location.

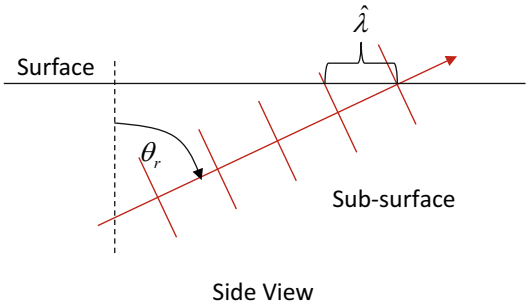

Fig. 4 Apparent wavelength elongation of bulk waves caused by oblique propagation

Energy Imaging

The entire wavefield is readily visualized as a movie, and although the viewer can obtain qualitative insights from the movie, it is desirable to obtain quantitative information similar to that which can found in a conventional ultrasonic C-scan. Individual snapshots are such an image, but they do not capture information from the entire wavefield. A straightforward alternative is to generate an energy image $E(x,y)$,

$$E(x,y) = \sum_{t=t_1}^{t_2} w^2(t,x,y), \tag{2}$$

where t_1 and t_2 are the start and stop times for a time window in which energy is accumulated.

If the data are broadband, it may be useful to first transform the time-windowed data into the frequency domain and accumulate energy in a defined frequency range. If $W(\omega,x,y)$ is the 1-D Fourier transform of the time-windowed wavefield, then the energy image corresponding to any desired frequency band can be directly computed in the frequency domain,

$$E(x,y) = \sum_{\omega=\omega_1}^{\omega_2} W^2(\omega,x,y), \tag{3}$$

where ω_1 and ω_2 are the start and stop radian frequencies ($\omega = 2\pi f$) for the frequency range over which energy is accumulated.

Figure 5 shows three energy images of the composite panel shown on the same 30 dB scale that were computed using three different time windows. The image computed using the full time window of 0 to 1800 μs clearly shows the impact damage as well as the shadowing effect of transducer #2, although the high-energy region around the source transducer dominates. The image computed using the narrow time window of 0 to 200 μs is similar although the shadowing effects of both the impact damage and transducer #2 are more evident. This time window was selected to ensure that the primary incident wave from the source transducer reached the lower right corner of the scan area so that the entire area of interest is interrogated but edge reflections are minimized. The third image was computed using the 200 to 1800 μs time window,

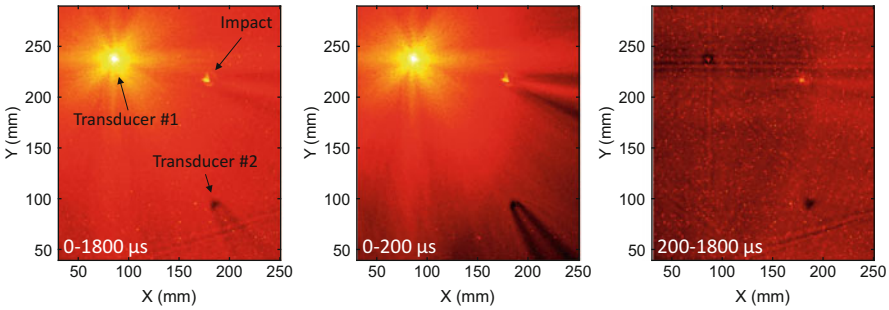

Fig. 5 Energy images of the composite panel specimen computed for three different time windows

which does not include the primary incident wave but does include multiple edge reflections. Each location on the panel is thus interrogated by multiple waves that are incident from different directions. Both transducers appear as anomalies of lower energy with no obvious shadowing, and the impact appears as a higher energy anomalous region because of energy trapping within the delamination. The noisy background is typical of laser vibrometer data and is caused by laser speckle that is more evident when signal levels are low. In general, energy imaging tends to highlight inhomogeneous regions where an otherwise smoothly varying energy field is disturbed, and is thus most effective for identifying anomalies in otherwise homogeneous parts.

Direct Arrival Imaging

A wavefield is typically recorded over a long enough time window for the waves to propagate over the entire region of interest. At all or some spatial locations, received signals typically include not only the direct arrival from the source but reflections and mode-converted signals from boundaries and other geometrical features of the specimen. An energy image that is constructed over a large time window includes all of these contributions, which can be useful since defects may be interrogated multiple times by reflected and scattered waves. A smaller time window focuses on the waves arriving directly from the source, but one window may not be optimal for all spatial locations.

An alternative approach is to create an energy image from only the direct arrival of the source wavefront, which is the first wave to interact with a specific spatial location. If the source is located at (x_s, y_s) and the image pixel is located at (x, y), the arrival time t_{arr} can be calculated as

$$t_{arr}(x,y) = \frac{\sqrt{(x - x_s)^2 + (y - y_s)^2}}{c_g} + t_{cal}, \tag{4}$$

where c_g is the group velocity and t_{cal} is a calibration offset time. An energy image can be calculated using Eq. (2) but with t_1 and t_2 being a function of x and y such that the time window encompasses the direct arrival:

$$t_1(x,y) = t_{\text{arr}}(x,y) - \Delta t/2 \text{ and } t_2(x,y) = t_{\text{arr}}(x,y) + \Delta t/2. \quad (5)$$

The total window width of Δt is set so that the time window for energy accumulation includes the directly arriving wave packet from the source. Here c_g is assumed to be constant, which may not be the case. If the specimen is anisotropic, then c_g would be a function of propagation direction. If the specimen is inhomogeneous, then c_g may be a function of position and it could be challenging to calculate the arrival time for each pixel. Direct arrival imaging highlights how the first arrival is perturbed by not only any inhomogeneity at the pixel location but also by the path of the wave from the source to that location.

Geometric spreading losses as well as material attenuation cause direct arrival amplitudes to decrease as a function of distance from the source. An amplitude correction can be applied to compensate for these losses,

$$E(x,y) = \sum_{t=t_1}^{t_2} w^2(t,x,y) \frac{d}{d_{\text{ref}}} e^{\alpha d}, \quad (6)$$

where d is the distance from the source to the point (x,y), d_{ref} is a reference distance, α is the attenuation, and the times are calculated as per Eq. (5).

Figure 6 shows three direct arrival images constructed for the composite panel assuming a constant group velocity of 1.38 mm/μs and for a time window of 10 μs. An additional calibration offset time of 2.2 μs was applied to ensure best tracking of the first arrival. Figure 6a was computed used the raw (non-envelope-detected) signals and no amplitude correction. Note the waviness in the lower part of the image, which is caused by signal peaks "rolling" through the time window due to dispersion (mismatched phase and group velocities). Figure 6b was computed from the envelope-detected signals, which removes the waviness but is otherwise very similar, and Fig. 6c applies a correction for geometric spreading but not material attenuation. All images are shown on a 30 dB scale normalized to the maximum for the image.

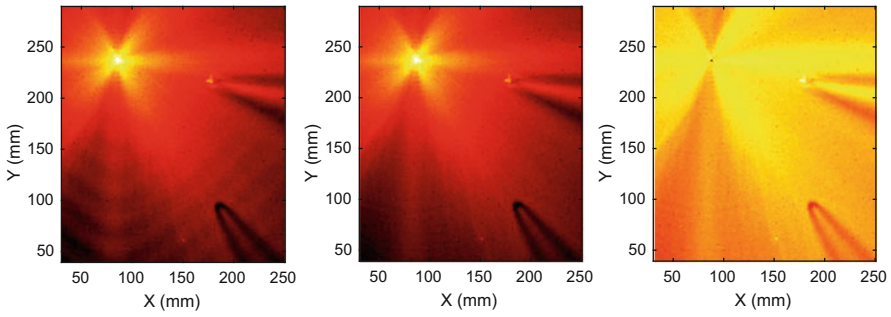

Fig. 6 Direct arrival images for the composite panel specimen. (**a**) Raw signals, no amplitude correction, (**b**) envelope-detected signals, no amplitude correction, and (**c**) envelope-detected signals, correction for geometric spreading

The direct arrival image of Fig. 6b is very similar to the energy image of Fig. 5b constructed using the narrow time window of 0 to 200 μs. This similarity is not surprising since the panel is nominally homogeneous except for the impact damage and affixed transducers. As can be seen in the snapshots of Fig. 2, there is little energy behind the direct arrival prior to the arrival of edge reflections. The direct arrival image of Fig. 6c includes a correction for geometric spreading, which evens out the background energy level to some extent. All three images of Fig. 6 show that the angular pattern of the incident wavefield is not uniform with lower energy in the ±90° directions and higher energy at 0° and 180°. These variations could be caused by transducer asymmetry, specimen anisotropy, or a combination of both.

Frequency-Wavenumber Analysis

Wavefield data are converted from the time-space domain to the frequency-wavenumber domain using either the 2-D Fourier transform (for line scans) or the 3-D Fourier transform (for area scans). Since data are acquired in both time and space, both temporal and spatial Nyquist criteria must be met to avoid aliasing. In the time domain, the sampling frequency must be more than twice that of the highest frequency present in the signals, which is the same as stating that the temporal sampling increment must be less than half of the shortest period. In reality, data are typically oversampled, at least in the laboratory, at five to ten times the Nyquist rate to provide a smooth representation of the signals. Since such digitizers are readily available for the ultrasonic frequency ranges typical for ultrasonic NDE and memory is relatively inexpensive, such oversampling is usually not a burden. Such is not the case, however, for spatial sampling. To meet the spatial Nyquist criterion, the spatial sampling increment must be less than half of the smallest wavelength of propagating waves. Since the acquisition time is proportional to the number of waveforms acquired, halving the spatial sampling increment quadruples the acquisition time for an area scan. If the spatial Nyquist criterion is not met, the data may still be useful but it will likely not be possible to apply frequency-wavenumber methods.

In two dimensions, the continuous Fourier transform is defined as

$$W(\omega,k) = \int_{-\infty}^{\infty} \int_{-\infty}^{\infty} w(t,r) e^{-i(kr-\omega t)} \, \mathrm{d}t \, \mathrm{d}r, \tag{7}$$

where r is the single spatial dimension, ω is the angular frequency, and k is the wavenumber. The angular frequency, wavenumber, and phase velocity are related by

$$c_\mathrm{p} = \frac{\omega}{k}. \tag{8}$$

In three dimensions, the continuous Fourier transform is

$$W(\omega, k_x, k_y) = \int_{-\infty}^{\infty} \int_{-\infty}^{\infty} \int_{-\infty}^{\infty} w(t,x,y) e^{-i\left(k_x x + k_y y - \omega t\right)} \, \mathrm{d}t \, \mathrm{d}x \, \mathrm{d}y, \tag{9}$$

and the wavenumber $k = \sqrt{k_x^2 + k_y^2}$. In practice, the discrete Fourier transform, rather than the continuous Fourier transform, is implemented using either the 2-D or 3-D fast Fourier transform (FFT) computational algorithm.

Figure 7 shows the 2-D frequency-wavenumber image of the guided wave signals shown in the B-scan of Fig. 3a for two different time windows. For both cases, a Hanning window is applied in both time and space to minimize spectral leakage. In Fig. 7a, a narrow time window of 0 to 80 μs is used that contains only the first arrivals of the two modes. It can be seen in this figure that the trajectories of both modes closely agree with the theoretical dispersion curves, which are superimposed on the image. A larger window of 0 to 300 μs is considered in Fig. 7b, and although the dispersion curves are still evident, the presence of the edge reflections adds considerable complexity to the frequency-wavenumber image. In particular, the apparent phase velocities of edge reflections are higher than the actual phase velocities when the measurement direction of the line scan is not coincident with the propagation direction. This issue, which only occurs for the 2-D Fourier transform, is illustrated in Fig. 8. The measured phase velocity $\hat{c}_\mathrm{p}$ is increased from that of the propagating waves by the cosine of the angle between the two directions, α:

$$\hat{c}_\mathrm{p} = \frac{c_\mathrm{p}}{\cos(\alpha)}. \tag{10}$$

The 3-D frequency-wavenumber domain is similar to that in 2-D but since an area scan includes all directions of propagation, there cannot be a mismatch between

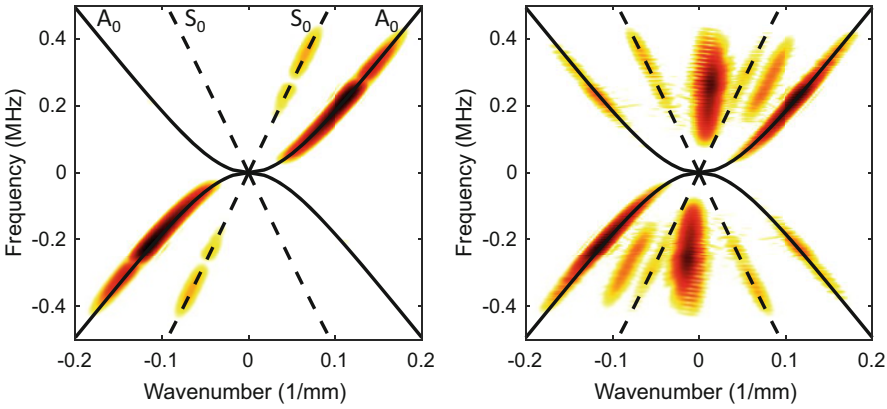

Fig. 7 Frequency-wavenumber representation of wavefield line scan data recorded from a 2.54 mm thick aluminum plate. (**a**) 80 μs window and (**b**) 300 μs window

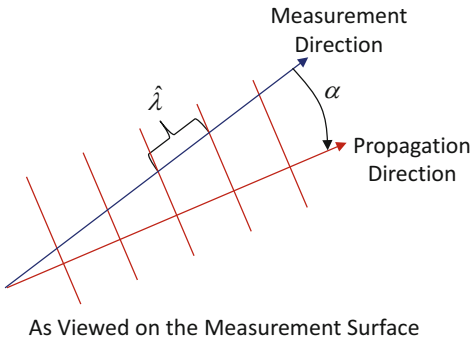

Fig. 8 Apparent wavelength elongation caused by a mismatch in measurement and propagation directions

the measurement and propagation directions. Each discrete point in the 3-D frequency-wavenumber domain has corresponding values of ω, k_x, and k_y. Recalling that $k = \sqrt{k_x^2 + k_y^2}$ and $c_\mathrm{p} = \omega/k$, each location also has a well-defined phase velocity. In addition, the wavenumber vector $\mathbf{k}$ points along the direction of propagation $\hat{\mathbf{k}}$:

$$\mathbf{k} = k_x \hat{\mathbf{e}}_x + k_y \hat{\mathbf{e}}_y \quad \text{and} \quad \hat{\mathbf{k}} = \frac{\mathbf{k}}{|\mathbf{k}|}. \tag{11}$$

Thus, each point also has a well-defined propagation direction.

Figure 9 shows frequency-wavenumber slices for three different propagation angles after taking the 3-D FFT of the composite panel data. The entire wavefield was preprocessed to reduce the total time window to 700 μs and smooth all edges in both time and space to avoid spectral leakage. These slices are similar to the one shown in Fig. 7a in that there is a dominant A_0-like slow mode and a much weaker S_0-like fast mode. The white line has a slope corresponding to a phase velocity of 2.5 mm/μs to serve as a reference; this line approximately separates the modes, although the actual mode shapes are not linear. The slope of the mode at a given frequency corresponds to the group velocity whereas the phase velocity is simply ω/k. The slope of the fast mode at $-45°$ is less than at $0°$ and $90°$, which is consistent with the fast mode wavefront shown in the snapshot of Fig. 2a. The slow mode is very slightly anisotropic but the group velocity of 1.38 mm/μs used for the direct arrival images of Fig. 6 matches well enough for accurate arrival time calculations within the region of interest for all propagation directions.

Figure 10 shows wavenumber-wavenumber (k_x–k_y) slices for three different frequencies. The white circle in each figure again corresponds to a phase velocity of 2.5 mm/μs. The nearly isotropic slow mode appears as the larger diameter approximately circular shape whereas the weaker and strongly anisotropic fast mode corresponds to a square-like shape inside the 2.5 mm/μs reference circle; it is not visible on the 100 kHz plot and is very faint on the other two plots.

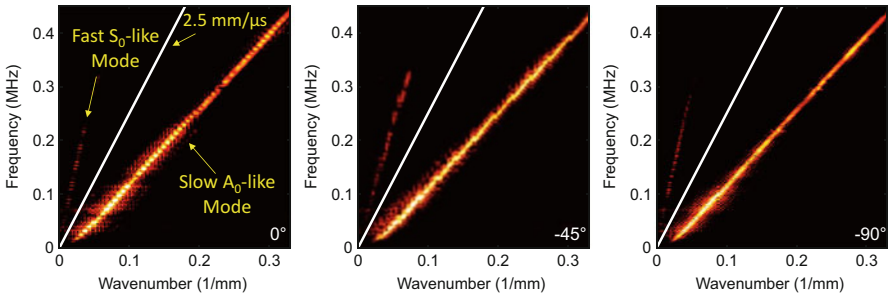

Fig. 9 Frequency-wavenumber slices in the 3-D Fourier domain for the composite panel specimen and three propagation directions. (**a**) 0°, (**b**) −45°, and (**c**) −90°

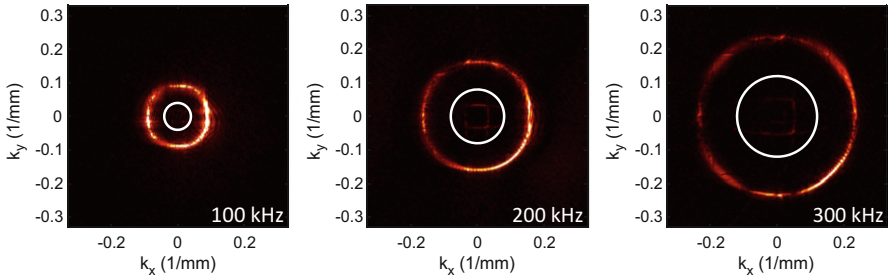

Fig. 10 Wavenumber-wavenumber slices in the 3-D Fourier domain for the composite panel specimen and three frequencies. (**a**) 100 kHz, (**b**) 200 kHz, and (**c**) 300 kHz

Frequency-Wavenumber Filtering

Direct visualization of wavefield data in the frequency-wavenumber domain is useful for understanding wave modes and overall propagation characteristics. But the real value of frequency-wavenumber analysis comes from filtering data in the Fourier domain and then transforming back to the time-space domain to analyze the filtered data (Ruzzene 2007; Michaels et al. 2011). Both phase velocity filtering and directional filtering are of interest to remove undesired phase velocities and propagation directions in the 3-D Fourier domain. An inverse FFT can then be applied to transform the filtered wavefield back to the time-space domain where it can be verified that the undesired wave components are no longer present.

As an example of phase velocity filtering, consider the various frequency-wavenumber domain slices shown in Figs. 9 and 10 for the composite panel. The weaker S_0-like mode is dominated by the much stronger A_0-like mode, but it can be enhanced by removing the stronger mode. Figure 11a, b shows two slices of a high-pass phase velocity filter that removes the strong mode and keeps the weak mode by setting a cutoff of 3.4 mm/μs. This filter additionally performs frequency-domain filtering by incorporating a bandpass filter from 50 to 500 kHz. The edges of the filter are smoothed to minimize spectral leakage. The snapshot of the filtered wavefield at

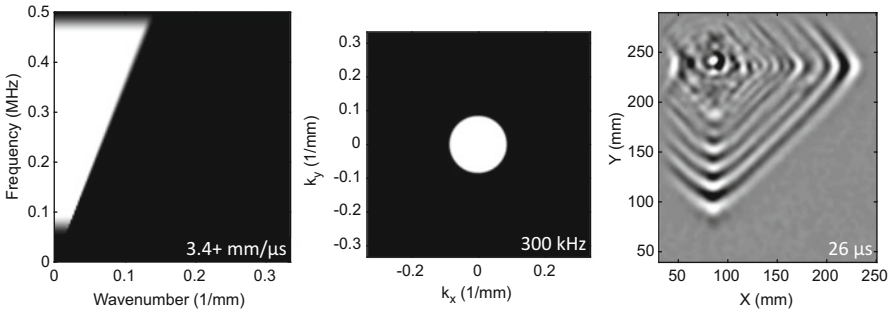

Fig. 11 Illustration of phase velocity filtering of composite panel data from 3.4 mm/μs and faster. (**a**) ω-k filter slice, (**b**) k_x-k_y filter slice, and (**c**) filtered snapshot at 26 μs

26 μs is shown in Fig. 11c where the anisotropic nature of this fast mode is much more evident than in the unfiltered snapshot of Fig. 2a. Although a linear phase velocity boundary was used here, the mode filters can also track the theoretical mode shapes as was done by Michaels et al. (2011) and Tian and Yu (2014).

Figure 12 illustrates directional filtering by removing all waves propagating between −135° and +135°, keeping only those leftward propagating waves between 135° and 225°. Figure 12a shows a snapshot of the original wavefield at 100 μs with the gray scale set to enhance visualization of waves scattered from the impact damage. The details of these scattered waves are largely obscured by the incident waves. After application of the directional filter shown in Fig. 12b, the snapshot of Fig. 12c clearly shows the backscattered waves from the impact damage as well as leftward propagating waves from the source transducer.

Guided Waves in a Composite Panel

The first case study continues the analysis of the wavefield data recorded from the composite panel as described in section "Acquiring and Visualizing Ultrasonic Wavefield Data." Results shown in section "Analyzing Ultrasonic Wavefield Data" indicate that the impact damage causes significant energy trapping whereas the effect of an attached transducer is to absorb energy. Figure 13 shows additional energy images computed as per Eq. (3) over the full time window of 1800 μs and for three different frequency ranges; all three images are shown on the same 30 dB scale. Figure 13a shows the image for a low-frequency band from 50 to 100 kHz. Although the image is dominated by the source transducer, both energy trapping and shadowing of the incident waves by the impact site are evident. The mid-frequency band image, from 150 to 200 kHz and shown in Fig. 13b, is also dominated by the source but displays a larger region of energy trapping and shows more of a disturbance of the wavefield from transducer #2; however, there is an overall higher background noise level. The highest band image shown, from 250 to 300 kHz and shown in Fig. 13c, continues the trend, but it is interesting to note that

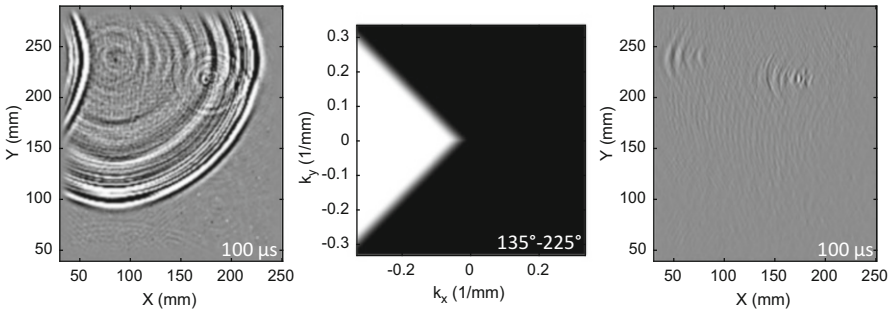

Fig. 12 Illustration of directional filtering of composite panel data from 135° to 225°. (**a**) Unfiltered snapshot at 100 μs, (**b**) directional filter, and (**c**) filtered snapshot at 100 μs

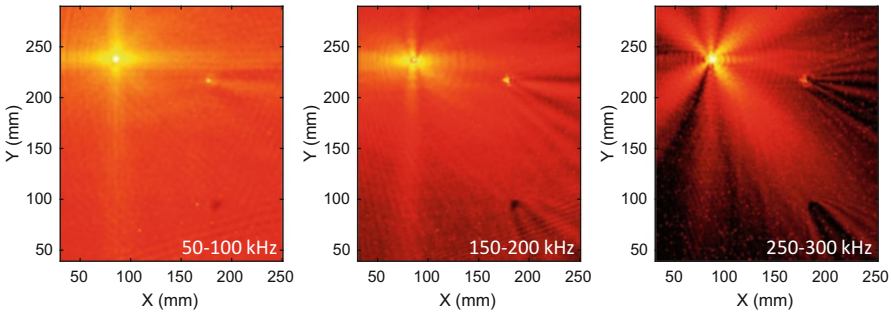

Fig. 13 Narrowband wavefield energy images from the composite panel. (**a**) 50–100 kHz, (**b**) 150–200 kHz, and (**c**) 250–300 kHz

the energy pattern around the source transducer has changed quite a bit. The difference in patterns suggests that the layup of the plate or possibly the transducer itself has caused a frequency-dependent directional pattern of the interrogating wavefront. Although these frequency-domain energy images are useful, they are not comparable to conventional C-scans in terms of their ability to characterize damage.

Frequency-wavenumber analysis methods provide another set of tools to identify damaged regions. Figures 9 and 10 in section "Frequency-Wavenumber Analysis" illustrate the process of applying the 3-D Fourier transform to the wavefield (after time windowing and edge smoothing) to map it from the time-space domain to the frequency-wavenumber domain. In the frequency-wavenumber domain, the slow mode appears ring-like and the fast mode squarish at each frequency with the slower mode corresponding to larger diameter rings and the faster mode lying within the slower mode ring. Most of the energy of the wavefield is contained in these modes, which are dominant in the undamaged plate and include incident waves, edge reflections, and scattered waves.

A strategy for identifying anomalous regions, which might be damage, is to look at the distribution of energy that is not associated with these modes. Figure 14a shows a

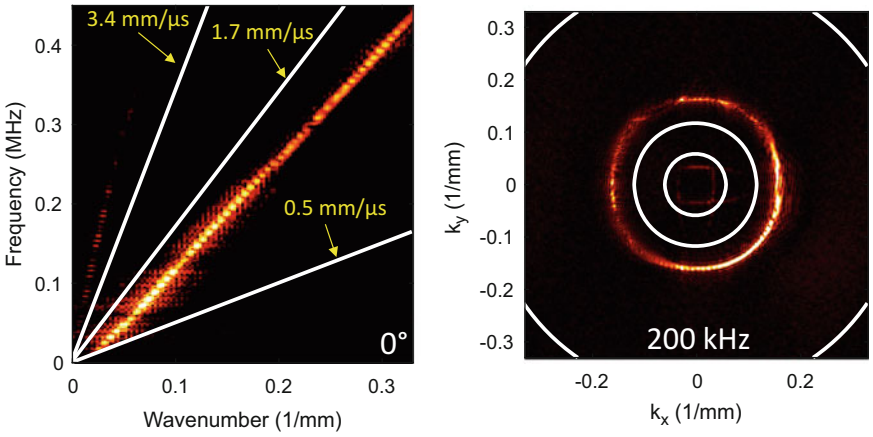

Fig. 14 2-D frequency-wavenumber slices showing phase velocity filtering boundaries. (**a**) Frequency-wavenumber slice at 0°, and (**b**) wavenumber-wavenumber slice at 200 kHz

frequency-wavenumber slice with the three white lines corresponding to phase velocities of 0.5, 1.7 and 3.4 mm/μs in order of increasing slope. The wedge-shaped region between 0.5 and 1.7 mm/μs bounds the dominant slow mode and the one between 3.4 mm/μs and infinity (vertical axis) bounds the weaker fast mode. The wedge between 1.7 and 3.4 mm/μs does not contain energy from either of the dominant modes; in fact, it appears to contain no energy at all, but that is not the case. Figure 14b shows a wavenumber-wavenumber slice at 200 kHz with the three circles corresponding to phase velocities of 0.5, 1.7, and 3.4 mm/μs in order of decreasing diameter.

As previously described in section "Frequency-Wavenumber Filtering," phase velocity filtering can be applied to obtain filtered wavefields corresponding to three ranges of phase velocities: 0.5 to 1.7 mm/μs for the dominant slow mode, 3.4 to ∞ mm/μs for the weaker fast mode, and 1.7 to 3.4 mm/μs for the so-called anomalous modes. Figure 11 shows the specific filter used for the fast mode, and similar filters were constructed for the other two ranges of phase velocity. Figure 15 shows energy images of these three wavefields, which confirm that the anomalous modes are indeed indicative of anomalies such as damage. The three indications on this image correspond to the site of impact damage and the two attached transducers, all of which are anomalies in the panel.

Wavefield data were also recorded over the same area using transducers #2 and #3 as sources, and "anomalous mode" images similar to that of Fig. 15c were generated from these two transducers. Figure 16 shows all three images after applying a 3×3 median filter to reduce the speckle noise. Although the background noise level is different for the three images, they are remarkably similar and unambiguously detect the impact damage. The attached transducers also appear as anomalies, which is expected since they perturb the wavefield.

The three images were "fused" together by averaging to yield a composite image as shown in Fig. 17a, also shown on a 30 dB scale. To evaluate the efficacy of the

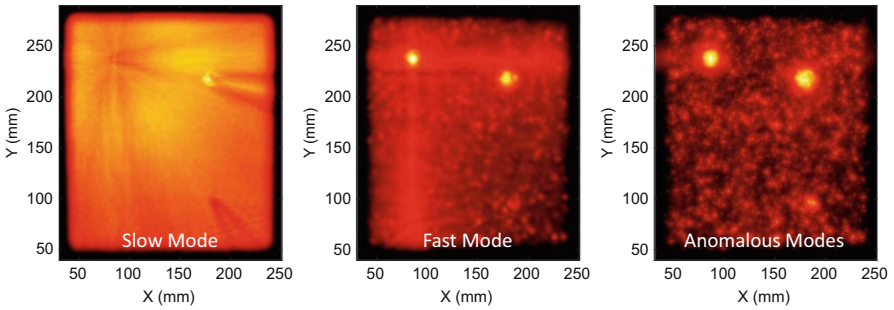

Fig. 15 Wavefield energy images after frequency-wavenumber filtering. (**a**) Slow mode, (**b**) fast mode, and (**c**) anomalous modes. Each image is shown on a 30 dB scale relative to its peak value

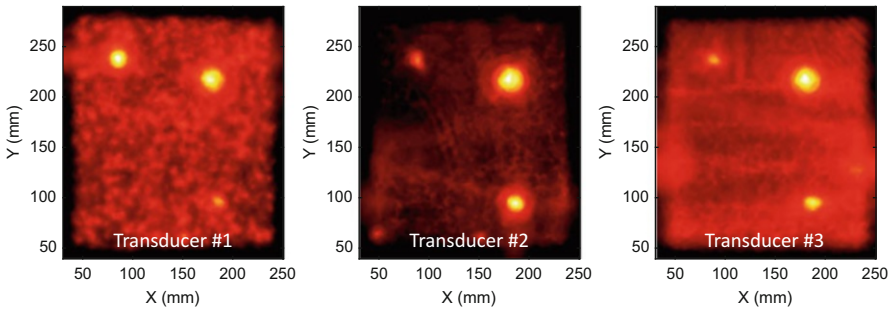

Fig. 16 Wavefield energy images after frequency-wavenumber filtering. (**a**) Slow mode, (**b**) fast mode, and (**c**) anomalous modes. Each image is shown on a 30 dB scale relative to its peak value

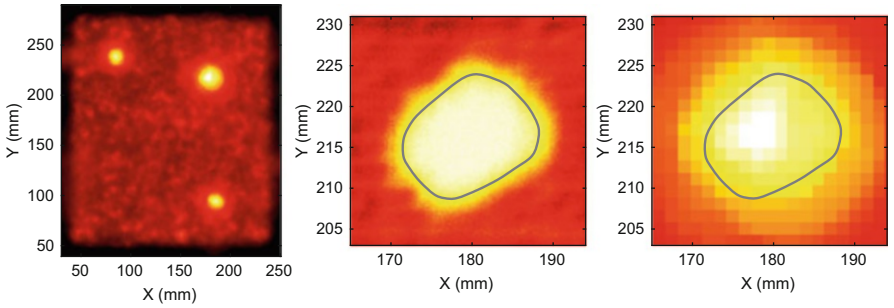

Fig. 17 (**a**) Fused "anomalous mode" energy image, (**b**) double through-transmission C-scan, and (**c**) zoomed energy image. The curves in (**b**) and (**c**) are identical for comparison

wavefield imaging method, it can be compared to a conventional immersion C-scan, which is shown in Fig. 17b. This image was obtained with a 10 MHz, 12.4 mm diameter, 100 mm focal length immersion transducer using the double through-transmission method. In this method, also called the reflectoplate method, signals are

generated and received in pulse-echo mode, but the gate is set to report the peak amplitude from a far-side reflecting plate. Note that the color bar is inverted so that the bright region corresponds to low signal amplitudes caused by the impact blocking the longitudinal wave. Figure 17c is a zoomed version of Fig. 17a over the same area as the C-scan was performed. The curve tracing the impact damage, which was hand-drawn to match the indication in the C-scan, is shown in both Fig. 17b, c. It matches well with the wavefield anomalous mode energy image despite the fact that the resolution is much coarser, the color scales are not strictly comparable, and the spatial alignment between the two scans is not perfect.

Guided Waves in a Bonded Plate

The second case study is that of guided waves propagating in a bonded aluminum plate; the experiment was originally described by Michaels and Michaels (2006). The specimen was constructed by bonding together two 1.5 mm thick aluminum plates with epoxy; the bond was intentionally fabricated with numerous air bubbles and an inconsistent thickness. As seen in the diagram of Fig. 18, the upper plate, which measured approximately 355 × 610 mm, was twice the size of the lower plate, which measured 355 × 305 mm. Four 12.5 mm diameter PZT disks were attached to the back side of the specimen, and transducer #1 was driven by an impulsive excitation to generate guided waves. The resulting wave motion was measured over the entire area at a spatial increment of 1.27 mm using a 400 kHz, 50 mm focal length, air-coupled transducer that was oriented normal to the upper specimen surface. Signals were sampled at 5 MHz over a 250 μs time window beginning at the

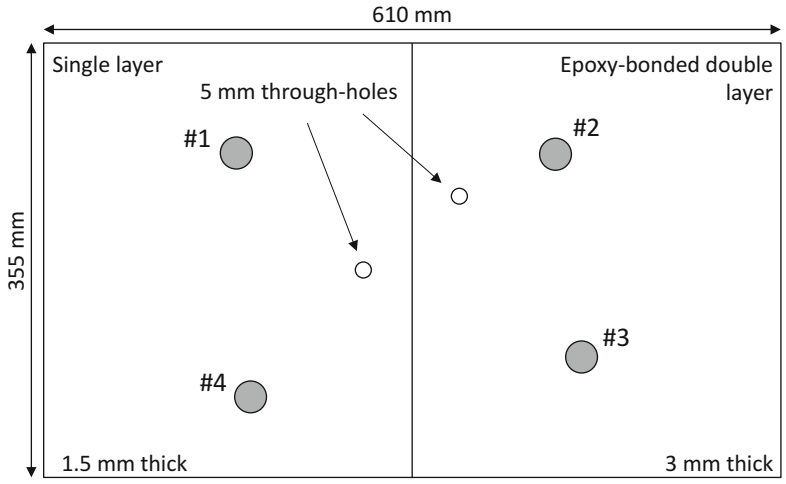

Fig. 18 Bonded plate specimen

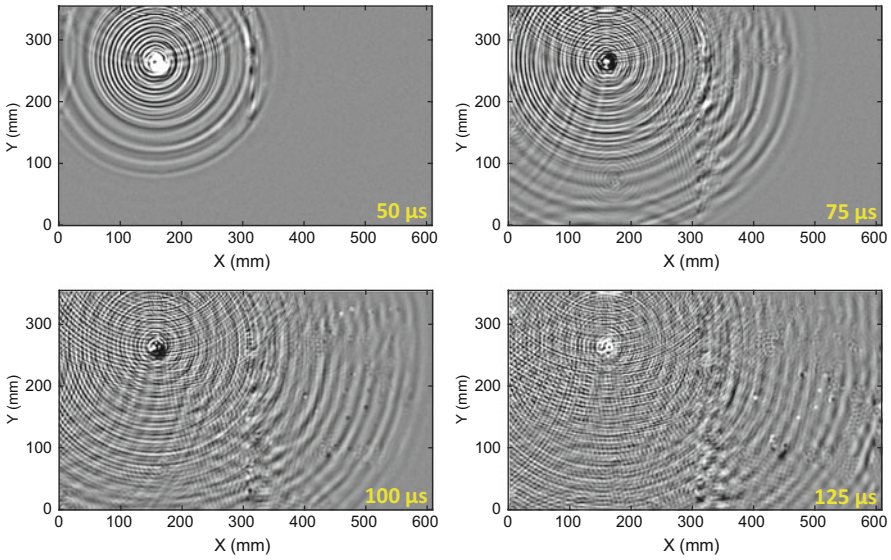

Fig. 19 Wavefield snapshots from the bonded plate specimen

first arrival of the airborne wave at the receiver. The total scan time was about 20 min for the 134,400 signals, which is less than 10 ms per point.

Figure 19 shows snapshots of the measured wavefield at four different times. The zero-time reference is the time of arrival of the first wave at the receiver when the transducer is directly above the transmitter; that is, the propagation time through the air has been subtracted. In the snapshot at 50 μs, the faster, longer wavelength S_0 mode can be seen to lead the circular wavefronts followed by the slower, shorter wavelength A_0 mode. As time progresses, the waves emanating from the source transducer appear to reverberate, which is actually due to the resonance of the narrowband air-coupled receiver. The waves can be seen to interact with the other attached transducers, the vertical boundary between the single plate on the left and the double layer on the right, and the various air bubbles in the epoxy layer. In addition, mode conversion from S_0 to A_0 at the attached transducers and the bond line can be readily observed. As time progresses, edge reflections cause the wavefield to become increasingly complicated, but also cause the epoxy layer air bubbles to become better delineated, primarily because of wave trapping within the bubbles.

Although the eye can readily discriminate most features of interest while playing the wavefield as a movie, it is more challenging to obtain a clear image of those features such as can be obtained by conventional ultrasonic imaging. Figure 20a shows a double-through-transmission C-scan of the entire specimen that was obtained with a 10 MHz, 12.4 mm diameter, 100 mm focal length immersion transducer. As expected, the bonding defects and the attached transducers can be clearly visualized as an almost complete loss of amplitude. Thickness variations are

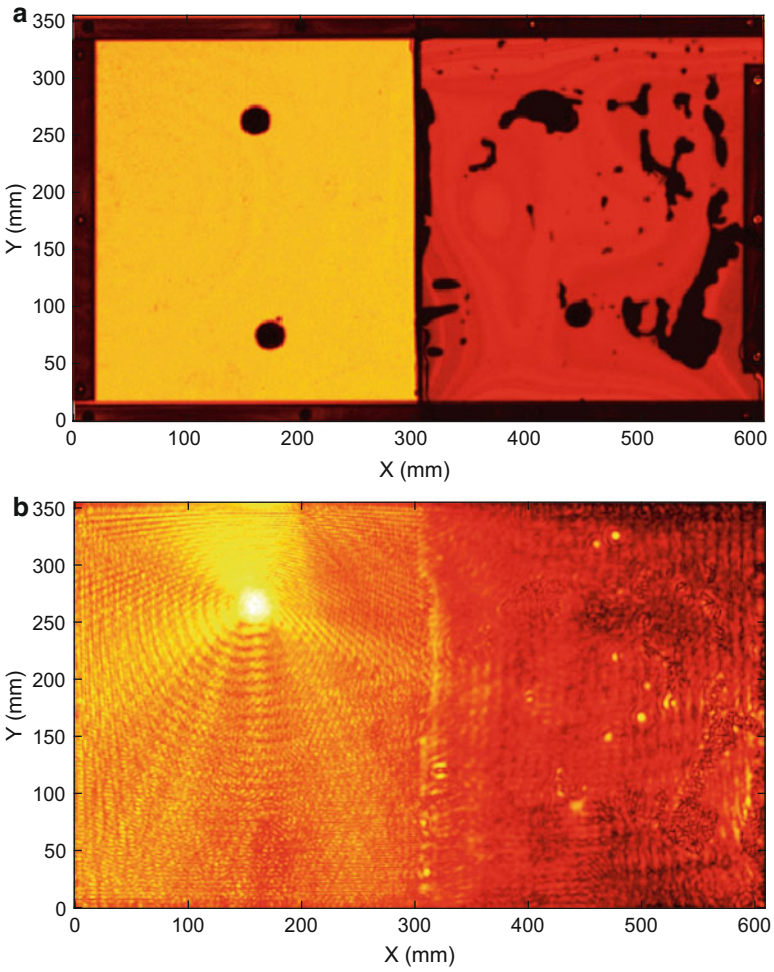

Fig. 20 (**a**) C-scan of bonded plate specimen, and (**b**) wavefield energy image

manifested as small changes in amplitude. The two through-holes were added after the C-scan was performed, so they do not appear in the image. Figure 20b shows a total energy image as obtained from the wavefield data for comparison; it is shown on a 30 dB scale. It might be expected that this image would highlight energy trapping in the bonding defects. However, although there are many indications in this image that correspond to the defects visible in the C-scan, most of them are not clearly delineated.

This wavefield does not lend itself to Fourier analysis for two main reasons. First, signals are saturated, particularly near the source transducer. Second, the reverberations of the receiver cause the wavefronts to appear to reverberate so that even if

modes and directions are separated, there is no resulting localized behavior in the time-space domain. Despite these complications, when viewing the wavefield movie, it can be seen that the leading edge of the faster S_0 mode has the clearest interaction with the specimen features since there is little or no interference with either the slower mode or edge reflections. Although the specimen is not homogeneous, the wave speed of the fast mode is similar for the two halves of the bonded plate (single layer versus double layer). Thus, a direct arrival image can be readily calculated using Eq. (5) with a constant group velocity to calculate the arrival time of the fast mode at any position (x, y) on the specimen. If the group velocity changed significantly from one side of the plate to the other, the arrival time could still be calculated but with a more complicated expression.

Figure 21 shows a side-by-side comparison of the C-scan and the arrival time image for the right side of the specimen. Direct arrival imaging is not as effective for the left side because of signal saturation. The parameters for the arrival time image are $c_g = 5.3$ mm/μs, $\Delta t = 10$ μs, and $t_{\text{cal}} = 20$ μs, and it is shown on a 20 dB scale for best comparison to the C-scan, whose color scale has been adjusted to increase the dynamic range. The direct arrival image is remarkably similar to the C-scan with almost all indications appearing on both images. One difference is that some of the small indications, which are presumably air bubbles in the epoxy, are manifested as higher energy indications in the direct arrival image whereas they are lower in the C-scan. Correction for geometrical spreading has been applied, although some energy reduction is still evident, and the expected shadowing of the direct arrival by transducers #2 and #3 can be seen.

The direct arrival image is surprisingly good, particularly considering that the wavelength of the S_0 mode is approximately 20 mm compared to about 0.6 mm for

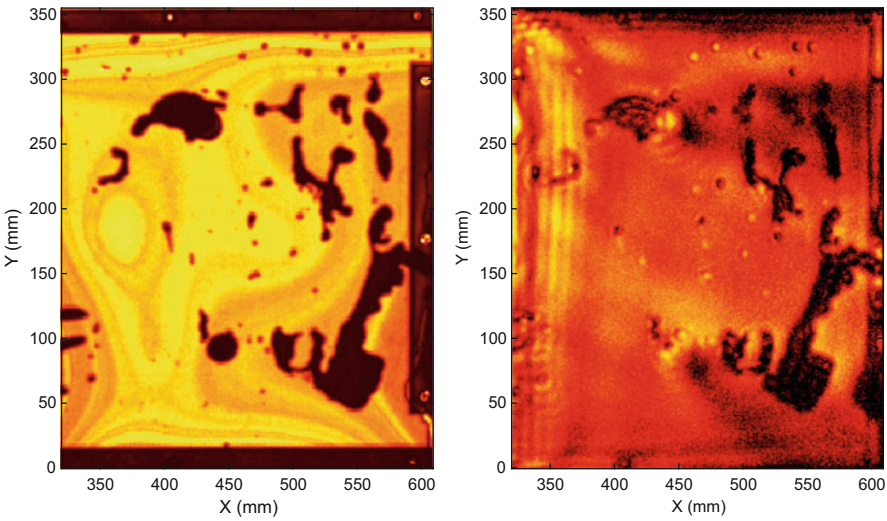

Fig. 21 Images of the right side of the bonded plate. (a) C-scan and (b) direct arrival image

the 10 MHz C-scan. One of the strengths of air-coupled wavefield scanning is the very fast acquisition time, which was about two orders of magnitude faster than would have been the case for a laser vibrometer. The direct arrival image highlights the effectiveness of this analysis method for bonding defects even when the data quality is compromised by reverberations.

Bulk Waves in an Aluminum Plate

The third case study applies wavefield imaging to investigate scattering of angle-beam shear waves from a notch emanating from a through-hole in an aluminum plate. Although wavefield imaging is particularly suited to the measurement of guided waves, it can also be applied to bulk waves, keeping in mind that the surface measurements are only a small portion of the total wavefield. The motivation of this study was to better understand scattering of angle-beam shear waves from back surface cracks with the long-term goal of improving inspection methods for such cracks.

Figure 22 illustrates the experimental configuration, in which a through-hole with a back-surface corner notch is interrogated with a conventional 5 MHz angle-beam shear wave probe with a nominal refracted angle of 56.8°. The thickness of the 6061 aluminum plate was 6.35 mm and the top surface had a mirror finish to improve the SNR. Wavefield data were acquired over a 30 × 30 mm square region centered about the 6.35 mm diameter through-hole using a laser Doppler vibrometer measuring out-of-plane displacement. The spatial increment in both x and y was 0.25 mm and the total scan time was about 3.5 h (about 1 s per point). The excitation was a 180 μs, 200 Vpp linear chirp from 1 to 10 MHz, and received signals were post-processed via deconvolution to obtain the equivalent response to a 2-cycle, 5 MHz, Hann-

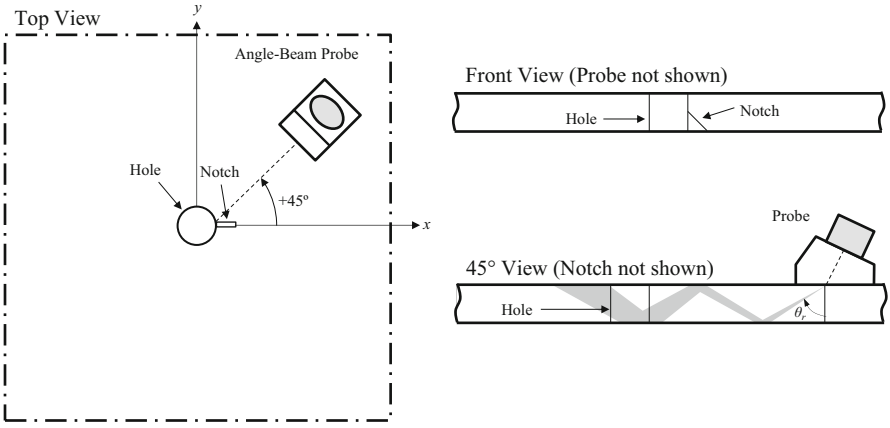

Fig. 22 Sketch of the aluminum plate specimen showing the through-hole, back-surface corner notch, and angle-beam probe (not to scale)

windowed tone burst (Michaels et al. 2013). Data sets were recorded both before and after introduction of the hand-cut back-surface corner notch that was initially 1 mm in length and was subsequently enlarged to 4 mm.

Figure 23 shows three wavefield snapshots at a time of 16.88 μs from the undamaged specimen and after introduction of the 2 mm and 4 mm notches. The through-hole boundary is shown on these and subsequent plots as an open circle. The waves are incident from the upper right as shown in Fig. 22. As can be seen in the plots, the wavefield has been spatially windowed to smooth the edges and also to remove the noisy signals obtained when scanning over the through-hole. A comparison of these snapshots clearly shows scattering from the notch, and an increase in scattering for the 4 mm notch as compared to the 2 mm notch. However, the wavefields are very complicated, consisting of incident waves, hole-scattered waves, and notch-scattered waves, and it is difficult to quantify the scattering from just the notch by simple spatial or temporal windowing. The hole-plus-notch is a compound scatterer and the waves scattered from the notch are particularly difficult to separate from those scattered from the hole.

The smallest wavelength in the data corresponds to the slowest wave, which is the Rayleigh wave whose nominal phase velocity is 2.9 mm/μs. Even though the angle-beam probe is designed to generate only shear waves, there are Rayleigh waves present in the incident wavefield (Dawson et al. 2016). Given the spatial increment of 0.25 mm, the minimum wavelength to avoid spatial aliasing is 0.5 mm, which corresponds to a maximum Rayleigh wave frequency of 5.8 MHz. To minimize Rayleigh wave aliasing while keeping as much information as possible, a simple bandpass filter was applied to each waveform by multiplication in the frequency domain with a 33% Tukey window from 0.5 to 6.5 MHz.

The analysis approach taken here generally follows that described by Dawson et al. (2017), and consists of the following main steps: (1) wavefield baseline subtraction to isolate notch-scattered waves, (2) 3-D frequency-wavenumber filtering to isolate shear waves, (3) extraction of radial B-scans at different angles relative to an observation point, and (4) accumulation of energy in the 2-D frequency-wavenumber domain to generate a scattering pattern. The end result captures

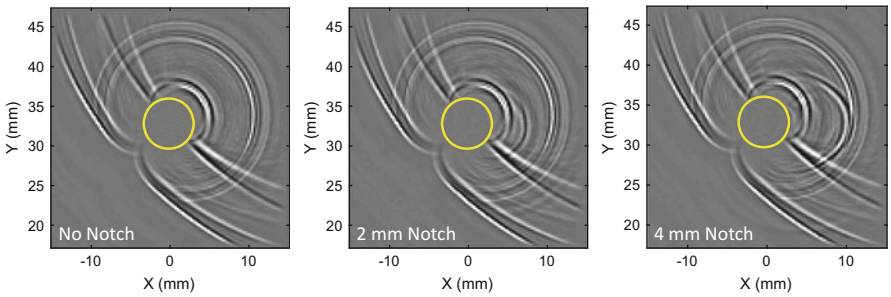

Fig. 23 Wavefield snapshots at 16.88 μs for (**a**) no notch, (**b**) 2 mm corner notch, and (**c**) 4 mm corner notch

scattered energy from all of the shear wave skips, where one skip refers to a full "bounce" from the top surface of the plate to the bottom surface and back to the top.

The first step of wavefield baseline subtraction, as its name implies, is the subtraction of two wavefields to yield a residual wavefield,

$$w_r(t,x,y) = w_c(t,x,y) - w_b(t,x,y), \tag{12}$$

where $w_c(x,y,t)$ is the current wavefield, $w_b(x,y,t)$ is the baseline wavefield, and $w_r(x,y,t)$ is the residual wavefield. Here the baseline wavefield is taken to be that recorded from the undamaged specimen (hole with no notch), and the current wavefield is after introduction and subsequent enlargement of the notch. Although wavefield baseline subtraction is straightforward in principle, in practice it is difficult to get acceptable results because it is virtually impossible to achieve perfect alignment between the current and baseline wavefields. Following the method developed by Dawson et al. (2016), each frame of the current wavefield is matched to a nearby frame of the baseline wavefield prior to subtraction where the baseline frame is spatially shifted to minimize the residual energy for each frame. Figure 24 shows residual wavefield snapshots at a time of 16.88 μs for the 2 mm, 3 mm, and 4 mm notch sizes; these snapshots are shown on the same gray scale as those of Fig. 23. Although some feedthrough of the incident and hole-scattered waves is evident, baseline subtraction is largely successful in extracting the notch-scattered waves. The expected increase in notch scattering as the notch size increases can be clearly seen.

The second step is to apply phase velocity filtering in the 3-D frequency-wavenumber domain to extract shear waves. There are both incident and hole-scattered Rayleigh waves present in the wavefield as well as hole- and notch-scattered longitudinal waves (Dawson et al. 2016). Since scattered shear waves are of interest, it is desirable to remove the Rayleigh and longitudinal waves. Although the bulk shear wave speed is well-known, as described in section "Phase and Group Velocities" the apparent phase velocity on the surface is faster than the bulk wave speed by a factor of $1/\sin(\theta_r)$, where θ_r is the refracted angle. Thus, the phase velocity limits for the phase velocity filter were set to the nominal shear and longitudinal wave speeds of 3.11 mm/μs and 6.32 mm/μs, respectively. Setting a higher upper limit would

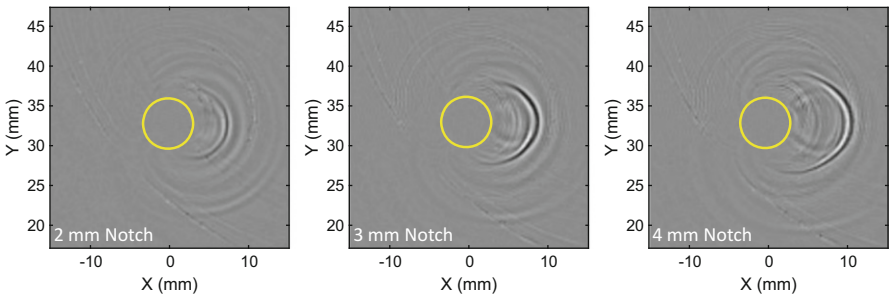

Fig. 24 Residual wavefield snapshots at 16.88 μs for three notch sizes. (**a**) 2 mm, (**b**) 3 mm, and (**c**) 4 mm

mean that some high-refracted-angle longitudinal waves could be included, and a smaller lower limit would include feedthrough of Rayleigh waves, whose nominal wave speed was 2.9 mm/μs. Figure 25 shows the three residual snapshots of Fig. 24 after phase velocity filtering, and it can be seen that they are significantly cleaner.

The third processing step is to extract radial B-scans from the residual wavefield relative to a specified reference point, which is illustrated in Fig. 26a. The residual wavefield snapshot in the background is that of Fig. 25c for the 4 mm notch. The reference point is designated by the "×" symbol, the hole is the solid circle, and the radial B-scan lines are the dotted lines, which are shown with a spacing of 22.5° for clarity. The reference point was chosen to be the hole-notch corner since the notch-scattered waves appear to approximately originate from this point. Since data are not measured inside the hole, the radial lines all begin outside of the hole and extend from 1 mm to 11 mm relative to the hole edge. Figure 26b shows the extracted radial B-scan for the 4 mm notch at an angle of 0°, and although there is some feedthrough of the incident waves, the outward propagating scattered waves dominate. Figure 26c shows the first quadrant of its frequency-wavenumber representation, which contains the forward (outward from the reference point) propagating waves.

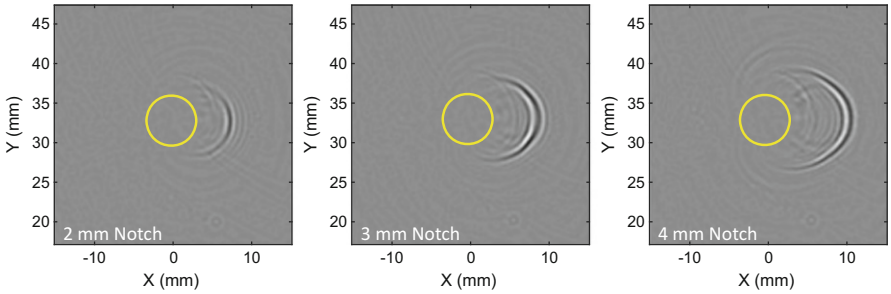

Fig. 25 Residual wavefield snapshots at 16.88 μs for three notch sizes after phase velocity filtering. (**a**) 2 mm, (**b**) 3 mm, and (**c**) 4 mm

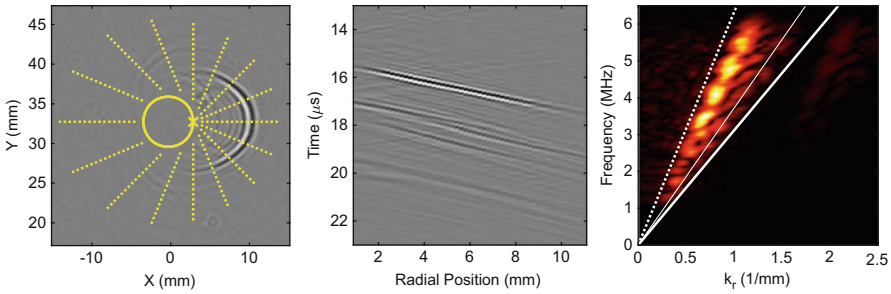

Fig. 26 Extraction and frequency-wavenumber analysis of radial B-scans. (**a**) Radial B-scan lines originating from the hole-notch corner, (**b**) radial B-scan at 0°, and (**c**) frequency-wavenumber representation of 0° radial B-scan

The heavy, solid line corresponds to the shear phase velocity of 3.11 mm/μs and the heavy dotted line to the longitudinal phase velocity of 6.32 mm/μs; the thinner line at 3.72 mm/μs corresponds to the nominal refracted angle of 56.8°. It can be seen that there is very little energy outside of the shear range because of the phase velocity filtering step. It is interesting to note that most of the energy is in the phase velocity range between 3.72 and 6.32 mm/μs, which corresponds to refracted angles smaller than the nominal (i.e., approaching normal incidence).

The final step is to accumulate energy in the frequency-wavenumber domain for each radial B-scan angle and for a specified phase velocity range. Different scattering patterns can be generated by specifying different ranges of phase velocities. Figure 27 shows 2, 3, and 4 mm notch scattering patterns computed for a phase velocity range of 3.62 to 3.82 mm/μs, which is a narrow range about the nominal phase velocity of 3.72 mm/μs (this range corresponds to refracted angles from 54.5° to 59.2°). These patterns all have narrow lobes with the largest lobe at about 240° (−120°), which corresponds to the notch shadowing the incident waves. All three patterns also have a strong but wider lobe at about 300° (−60°) and a third smaller lobe in the backscattered direction at close to +45°. Although the strength of all three lobes increases with notch size, their relative sizes change with the 2 mm notch having more nearly equal lobes than the 3 mm and 4 mm notches.

Figure 28 shows patterns for a broader but higher range of phase velocities, 4.4 to 6.3 mm/μs, which corresponds to a refracted angle range of 30–45°. These refracted angles are not present in the incident waves, at least not to a large degree, and are likely generated via diffraction from the notch edge or corner. The resulting scattering patterns are not as directional as those from the narrow range of phase velocities, which is consistent with the expected more omnidirectional scattering from a sharp discontinuity.

The methodology shown here for estimating scattering patterns is very general, and although applied here to bulk waves, is completely applicable to guided waves. In fact, its application to guided waves is more straightforward because there is no modal ambiguity as there is for shear and longitudinal bulk waves and it is easier to avoid spatial aliasing because of the generally larger wavelengths.

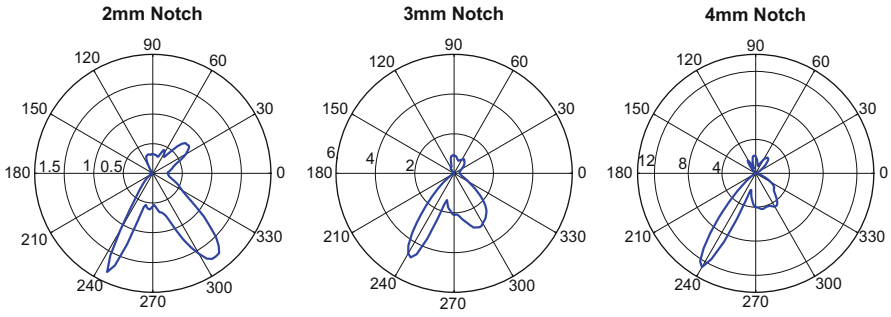

Fig. 27 Shear scattering patterns for a narrow range of phase velocities about the nominal refracted angle. (**a**) 2 mm notch, (**b**) 3 mm notch, and (**c**) 4 mm notch

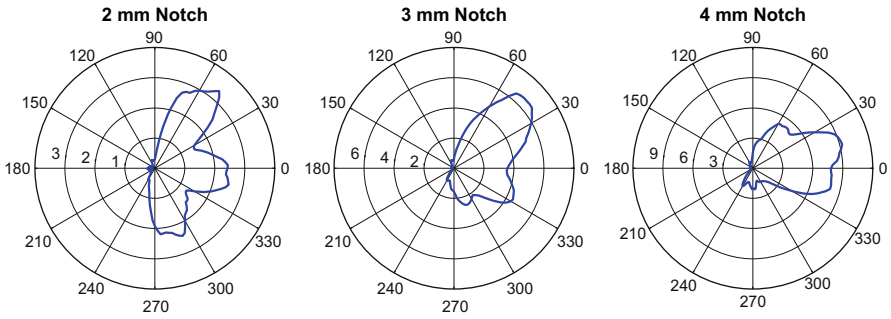

Fig. 28 Shear scattering patterns for a range of phase velocities corresponding to refracted angles of 30–45°. (**a**) 2 mm notch, (**b**) 3 mm notch, and (**c**) 4 mm notch

Additional Wavefield Methods

In addition to the wavefield methods shown here, there are many others that have been developed to address specific inspection problems. Several of these are reviewed in this section. In terms of visualization, a method similar to direct arrival imaging tracks a point of constant phase on the wavefield to image its variations over a region of interest. Unlike direct arrival imaging, the phase velocity must be used to track the wave crest instead of the group velocity. Michaels and Michaels (2007) called this method "wave crest amplitude analysis" and applied it to guided wave imaging of both simulated corrosion and notches in aluminum plates. Köhler et al. (2012) similarly tracked a crest on the wavefront of skimming longitudinal waves to map grain boundaries in an austenitic stainless steel weld.

Several analysis methods exploit the idea of anomalies in guided wavefields. Lee et al. (2012) proposed a time-space domain method whereby adjacent waves are time-aligned and subtracted to identify wavefield anomalies. Harb and Yuan (2016) applied frequency-wavenumber filtering to separate the wavefield into forward and backward propagating waves and applied a zero-lag cross-correlation method to identify anomalous backscattering caused by damage. Park et al. (2014) defined a standing wave filter based upon directional filtering and applied it to identify damage.

It is also possible to identify and characterize damage-induced anomalies in the wavenumber domain. Rogge and Leckey (2013) performed a local wavenumber analysis to not only detect impact damage in composites but to also estimate the depth of the impact. Flynn et al. (2013) similarly applied local wavenumber methods to estimate both wall thinning in metallic specimens and the depth of impact damage in composites. Kudela et al. (2015) performed wavenumber-wavenumber filtering in the spatial 2-D Fourier domain at each time slice to extract anomalous wavenumbers and then mapped each slice back to the spatial domain to identify damage. Yu et al. (2015) also noted the generation of anomalous wavenumbers by discontinuities and applied filtering using a short-space Fourier transform method to identify damage.

All of these methods illustrate the potential of wavefield imaging for a wide variety of inspection problems, but do not specifically address the typically very long scan times required for high-resolution measurements. Using air-coupled receivers is one possible solution which has the additional advantage of straightforward integration with conventional automated ultrasonic scanning systems but with the disadvantage of reduced data quality. A hardware-based approach is to use multi-point LDVs to measure multiple signals simultaneously (Kilpatrick and Markov 2010); such systems are in development but are not yet commercially available.

Another approach to address the scan time problem is to develop analysis methods that require fewer signals. Tian et al. (2016) proposed a "global-local" approach whereby the LDV system first acts as a receiver array to record a small number of signals that are used to construct a delay-and-sum image of a large area. Locations with anomalies are then targeted for high-resolution local scans, avoiding having to scan the entire specimen with a high resolution. Mesnil and Ruzzene (2016) took the approach of recording a small number of randomly distributed measurements and applying sparse reconstruction methods to locate both the actual source and secondary sources of waves that explain the measurements. These secondary sources are structural anomalies, or possible defects. Harley and Chia (2018) also considered a small number of randomly distributed measurements and used sparse reconstruction methods to estimate the damage-free wavefield. Residual signals at these random locations are then used to construct an image of damage.

One other promising approach to increase the speed of wavefield measurements is to apply a continuous excitation to generate a steady state wavefield at a constant frequency and measure the amplitude and phase with an LDV. Local wavenumber methods can then be applied to detect anomalies. Goodman et al. (2014) demonstrated this method to assess material distributions inside storage cylinders and achieved scan times of less than 10 s. Mesnil et al. (2016) similarly used continuous excitations to assess delaminations in composites, which reduced scan times from about 3 h to 10 min.

Summary

There is no question that wavefield imaging is playing a critical role in understanding how ultrasonic waves propagate and interact with both damage and structural features, particularly for guided waves. The specific applications and methods shown here are representative of what can be achieved with UWI but are by no means a comprehensive treatment. Clearly UWI is moving from being a powerful laboratory tool to an effective NDE method.

Despite this demonstrated effectiveness, the practicality of wavefield imaging still must be addressed. There are at least three closely related obstacles that must be overcome for wavefield imaging to be implemented in the field: (1) scan time, (2) data quality, and (3) data analysis methods.

In terms of scan time, there are several approaches being considered to address this issue as discussed in section "Additional Wavefield Methods." Although the time-consuming LDV-based systems that record transient signals will likely serve as the

"gold standard" for some time, clearly there are other approaches, both hardware and software, that can be brought to bear to reduce scan time to more practical values.

Data quality, which is closely related to scan time, is also an issue. The quality of laser vibrometer data can always be improved by more signal averaging at the expense of scan time. Data quality is very dependent upon surface optical reflectivity, which is often improved in the laboratory by applying reflective tape or paint. However, disturbing the surface removes one of the primary advantages of wavefield imaging over conventional ultrasonic NDE methods, which require couplant. Using a continuous excitation significantly improves the data quality at the frequency(ies) being excited because it is possible to inject much more energy than a pulsed excitation, but this type of excitation limits analysis options.

Ultimately the success of wavefield imaging as an NDE method will depend upon the data analysis methods. Unlike conventional ultrasonic imaging, in which both transmitter and receiver are locally scanned to map discontinuities, in UWI the presence of either a defect or benign feature affects the global wavefield, not just measurements in the vicinity of the defect or feature. It is definitely challenging to extract local information despite global disturbances, and although research efforts thus far have been moderately successful in doing so, the efficacies of the various methods need to be quantified for a wide variety of structures and defects. Most, if not all, of the proposed analysis methods have in common the idea of recognizing anomalies in the wavefield that are caused by damage. This approach, which is similar to that of conventional UT inspections, works well when most of the specimen is homogeneous, but may fail for more complicated structures.

The main competition for UWI is conventional ultrasonic testing (UT). There needs to be a compelling reason to use UWI, and its noncontact nature is likely to be an important part of that reason. Another attractive feature of UWI is that only one-sided access is needed. Even if the quality of the inspection is not as good as can be achieved with conventional UT, if the overall inspection time is less, including any required disassembly and reassembly, UWI could be preferred. The future deployment of SHM systems may be the driving force to move wavefield imaging out of the lab and into the field.

Acknowledgments The first case study was supported by Advanced Systems & Technology, Inc., Irvine, CA, as part of a NASA SBIR Phase II Award, Contract No. NNX15CL26C, Dr. Cara Leckey, program manager. The third case study was sponsored by the Air Force Research Laboratory, Contract No. FA8650-10-D-5210, Dr. Eric Lindgren, program manager.

References

An YK, Park B, Sohn H (2013) Complete noncontact laser ultrasonic imaging for automated crack visualization in a plate. Smart Mater Struct 22:025022 (10pp)

Dawson AJ, Michaels JE, Michaels TE (2016) Isolation of ultrasonic scattering by wavefield baseline subtraction. Mech Syst Signal Process 70–71:891–903

Dawson AJ, Michaels JE, Kummer JW, Michaels TE (2017) Quantification of shear wave scattering from far-surface defects via ultrasonic wavefield measurements. IEEE Trans Ultrason, Ferroelect Freq Control 64(3):590–601
Flynn EB, Chong AY, Jarmer GJ, Lee JR (2013) Structural imaging through local wavenumber estimation of guided waves. NDT&E Int 59:1–10
Gannon A, Wheeler E, Brown K, Flynn E, Warren W (2015) A high-speed dual-stage ultrasonic guided wave system for localization and characterization of defects. Conf Proc Soc Exp Mech Ser 7:123–136
Goodman D, Rowland K, Smith S, Miller K, Flynn E (2014) Non-destructive examination of multiphase material distribution in uranium hexafluoride cylinders using steady-state laser Doppler vibrometry. Conf Proc Soc Exp Mech Ser 5:81–88
Hall G (1977) Ultrasonic wave visualization as a teaching aid in non-destructive testing. Ultrasonics 15(2):57–69
Harb MS, Yuan FG (2016) Damage imaging using non-contact air-coupled transducer/laser Doppler vibrometer system. Struct Health Monit 15(2):193–203
Harley JB, Chia CC (2018) Statistical partial wavefield imaging using Lamb wave signals. Struct Health Monit 17(4):919–935
Kilpatrick JM, Markov VB (2010) Full-field laser vibrometer for instantaneous vibration measurement and non-destructive testing. Key Eng Mater 437:407–411
Köhler B, Barth M, Krüger P, Schubert F (2012) Grain structure visualization with surface skimming ultrasonic waves detected by laser vibrometry. Appl Phys Lett 101:074101 (3pp)
Kudela P, Radzieński M, Ostachowicz W (2015) Identification of cracks in thin-walled structures by means of wavenumber filtering. Mech Syst Signal Process 50–51:456–466
Lee JR, Chia CC, Park CY, Jeong H (2012) Laser ultrasonic anomalous wave propagation imaging method with adjacent wave subtraction: algorithm. Opt Laser Technol 44:1507–1515
Lee JR, Sunuwar N, Park CY (2014) Comparative analysis of laser ultrasonic propagation imaging system with capacitance and piezoelectric air-coupled transducers. J Intell Mater Syst Struct 25(5):551–562
Mesnil O, Ruzzene M (2016) Sparse wavefield reconstruction and source detection using compressed sensing. Ultrasonics 67:94–104
Mesnil O, Yan H, Ruzzene M, Paynabar K, Shi J (2016) Fast wavenumber measurement for accurate and automatic location and quantification of defect in composite. Struct Health Monit 15(2):223–234
Michaels JE (2017) Ultrasonic wavefield imaging: research tool or emerging NDE method? In: Chimenti DE, Bond LJ (eds) Review of progress in quantitative nondestructive evaluation, vol 36. AIP conference proceedings 1806 (020001, 14pp)
Michaels TE, Michaels JE (2006) Integrated monitoring and inspection with attached ultrasonic transducers. In: Kundu T (ed), Proceedings of the SPIE, vol 6177, 61770E (12pp)
Michaels TE, Michaels JE (2007) Monitoring and characterizing corrosion in aluminum using Lamb waves and attached sensors. In: Kundu T (ed) Proceedings of the SPIE, vol 6532, 65321G (11pp)
Michaels TE, Michaels JE, Ruzzene M (2011) Frequency-wavenumber domain analysis of guided wavefields. Ultrasonics 51:452–466
Michaels JE, Lee SJ, Croxford AJ, Wilcox PD (2013) Chirp excitation of ultrasonic guided waves. Ultrasonics 53:265–270
Nishizawa O, Satoh T, Lei X, Kuwahara Y (1997) Laboratory study of seismic wave propagation in inhomogeneous media using a laser Doppler vibrometer. Bull Seismol Soc Am 87(4):809–823
Park B, An YK, Sohn H (2014) Visualization of hidden delamination and debonding in composites through noncontact laser ultrasonic scanning. Compos Sci Technol 100:10–18
Rogge MD, Leckey CAC (2013) Characterization of impact damage in composite laminates using guided wavefield imaging and local wavenumber domain analysis. Ultrasonics 53:1217–1226
Rose JL (1999) Ultrasonic waves in solid media. Cambridge University Press, Cambridge, UK
Ruzzene M (2007) Frequency-wavenumber domain filtering for improved damage visualization. Smart Mater Struct 16:2116–2129

Tian Z, Yu L (2014) Lamb wave frequency-wavenumber analysis and composition. J Intell Mater Syst Struct 25(9):1107–1123

Tian Z, Yu L, Leckey C (2016) Rapid guided wave delamination detection and quantification in composites using global-local sensing. Smart Mater Struct 25:085042 (11pp)

Wyatt RC (1972) Visualization of pulsed ultrasound using stroboscopic photoelasticity. Non-Destr Test 5(6):354–358

Yu L, Tian Z, Leckey CAC (2015) Crack imaging and quantification in aluminum plates with guided wave wavenumber analysis methods. Ultrasonics 62:203–212